

Efficient characterization of the coupler spectrum via sideband driving in superconducting qubits

Jianwen Xu(徐建文), Ruonan Guo(郭若男), Wen Zheng(郑文), Yu Zhang(张钰), Jie Zhao(赵杰), Zhiguo Huang(黄智国), Jingwei Wen(闻经纬), Runqing Zhang(张润清), Shaoxiong Li(李邵雄), Xinsheng Tan(谭新生), and Yang Yu(于扬)

Citation: Chin. Phys. B, 2025, 34 (**11**): 110302. DOI: 10.1088/1674-1056/ae00b0
http://cpb.iphy.ac.cn; http://iopscience.iop.org/cpb

What follows is a list of articles you may be interested in

In-situ deposited anti-aging TiN capping layer for Nb superconducting quantum circuits

Hao-Ran Tao(陶浩然), Lei Du(杜磊), Liang-Liang Guo(郭亮亮), Yong Chen(陈勇), Hai-Feng Zhang(张海峰), Xiao-Yan Yang(杨小燕), Guo-Liang Xu(徐国良), Chi Zhang(张 驰), Zhi-Long Jia(贾志龙), Peng Duan(段鹏), and Guo-Ping Guo(郭国平)

Chin. Phys. B, 2024, 33 (**9**): 090310. DOI: 10.1088/1674-1056/ad6a3c

orrection of microwave pulse reflection by digital filters in superconducting quantum circuits

Liang-Liang Guo(郭亮亮), Peng Duan(段鹏), Lei Du(杜磊), Hai-Feng Zhang(张海峰), Hao-Ran Tao(陶浩然), Yong Chen(陈勇), Xiao-Yan Yang(杨小燕), Chi Zhang(张驰), Zhi-Long Jia(贾志龙), Wei-Cheng Kong(孔伟成), Zhao-Yun Chen(陈昭昀), and Guo-Ping Guo(郭国平)

Chin. Phys. B, 2024, 33 (**9**): 090303. DOI: 10.1088/1674-1056/ad5d98

Quantum simulation of lattice gauge theories on superconducting circuits: Quantum phase transition and quench dynamics

Zi-Yong Ge(葛自勇), Rui-Zhen Huang(黄瑞珍), Zi-Yang Meng(孟子杨), and Heng Fan(范桁)

Chin. Phys. B, 2022, 31 (**2**): 020304. DOI: 10.1088/1674-1056/ac380e

Universal quantum control based on parametric modulation in superconducting circuits

Dan-Yu Li(李丹宇), Ji Chu(储继), Wen Zheng(郑文), Dong Lan(兰栋), Jie Zhao(赵杰), Shao-Xiong Li(李邵雄), Xin-Sheng Tan(谭新生), and Yang Yu(于扬)

Chin. Phys. B, 2021, 30 (**7**): 070308. DOI: 10.1088/1674-1056/ac01c3

Interaction induced non-reciprocal three-level quantum transport

Sai Li(李赛), Tao Chen(陈涛), Jia Liu(刘佳), and Zheng-Yuan Xue(薛正远)

Chin. Phys. B, 2021, 30 (**6**): 060314. DOI: 10.1088/1674-1056/abee0c

---

RAPID COMMUNICATION

Efficient characterization of the coupler spectrum via sideband driving in superconducting qubits

Jianwen Xu(徐建文)[1,2,3,†], Ruonan Guo(郭若男)[1,2,3,†], Wen Zheng(郑文)[1,2,3,‡], Yu Zhang(张钰)[1,2,3], Jie Zhao(赵杰)[1,2,3], Zhiguo Huang(黄智国)[4], Jingwei Wen(闻经纬)[4], Runqing Zhang(张润清)[4], Shaoxiong Li(李邵雄)[1,2,3,5,6], Xinsheng Tan(谭新生)[1,2,3,5,6], and Yang Yu(于扬)[1,2,3,5,6,§]

[1] *National Laboratory of Solid State Microstructures, School of Physics, Nanjing University, Nanjing* 210093, *China*
[2] *Shishan Laboratory, Nanjing University, Suzhou* 215163, *China*
[3] *Jiangsu Key Laboratory of Quantum Information Science and Technology, Nanjing University, Suzhou* 215163, *China*
[4] *China Mobile (Suzhou) Software Technology Company Limited, Suzhou* 215163, *China*
[5] *Synergetic Innovation Center of Quantum Information and Quantum Physics, University of Science and Technology of China, Hefei* 230026, *China*
[6] *Hefei National Laboratory, Hefei* 230088, *China*

(Received 2 July 2025; revised manuscript received 15 August 2025; accepted manuscript online 29 August 2025)

Fabrication-friendly superconducting qubits continue to be a leading candidate for scalable quantum computing. Recent developments in tunable couplers have significantly advanced the progress toward practical quantum processors. However, high-performance quantum control, particularly two-qubit gates, depends on the delicate tuning of the coupler spectrum, as misalignment can lead to undesirable phenomena such as frequency crowding, which may cause errors including state leakage. Here, we propose an efficient method for characterizing the coupler spectrum through sideband drivings, obviating the need for additional components in current quantum processors. We demonstrate this technique experimentally by employing both continuous-wave and pulsed measurement protocols, successfully extracting the coupler spectrum. Furthermore, by utilizing the measured coupler spectrum, we calibrate the frequency dependence of the effective coupling strength between two qubits linked by the coupler. The proposed approach offers significant practical benefits, enabling the efficient characterization of the coupler spectrum in existing quantum architectures, thus paving the way for enhanced quantum control and scalability.

Keywords: superconducting quantum circuits, tunable coupler, sideband driving

PACS: 03.67.Lx, 85.25.Dq

DOI: 10.1088/1674-1056/ae00b0 **CSTR:** 32038.14.CPB.ae00b0

1. Introduction

The introduction of tunable couplers has enabled high-fidelity control to be achieved in both single-qubit and two-qubit operations[1–9] for superconducting quantum circuits.[10–12] This advancement has progressed in superconducting qubits through a series of significant milestones,[13–16] driving the field towards the development of large-scale, fault-tolerant quantum computers.[17–23] Of particular importance is the proposal of the transmon–coupler–transmon architecture,[1] which, combined with cutting-edge nanofabrication techniques,[24–31] has made it possible to delicately manipulate qubits whose operational parameters closely match theoretical designs. This achievement has been crucial in enabling the realization of high-performance quantum processors.[13–16,32–35]

Additionally, to address the significant resource overhead in quantum tasks such as quantum error correction,[36–41] which arises from the limited connectivity specific to transmon qubit,[42,43] the design of couplers with various coupling ranges for hardware-efficient quantum processors has become one of the current ongoing explorations.[44–51] This trend, in turn, imposes stringent requirements on the design, fabrication, and control of couplers, such as addressing challenges related to frequency crowding and control crosstalk during operations.[52] Consequently, there is a growing need for more efficient characterization of coupler performance, particularly in the spectral characterization, to support the scalable development of superconducting quantum processors.

Efficient characterization of the coupler spectrum is a critical component for the precise calibration of multi-qubit crosstalk,[52–54] waveform distortion,[55] and quantum gate operations.[56] By exploiting the spectral properties of the coupler, high-performance quantum manipulation can be achieved through targeted parameter tuning, which significantly enhances the reliability, fidelity, and overall operational efficiency of quantum circuits. For efficient characterization, the

[†]These authors contributed equally to this work.
[‡]Corresponding author. E-mail: zhengwen@nju.edu.cn
[§]Corresponding author. E-mail: yuyang@nju.edu.cn

© 2025 Chinese Physical Society and IOP Publishing Ltd. All rights, including for text and data mining, AI training, and similar technologies, are reserved.

first consideration involves direct readout via a dedicated resonator integrated with the coupler, providing direct spectral measurements. The second approach takes advantage of the residual coupling between the coupler and its associated qubit readout resonator. However, the former necessitates additional structural elements, complicating the current structure. On the other hand, the latter features a weak resonator–coupler interaction strength, leading to reduced readout contrast and bandwidth limitations.

A more sophisticated approach exploits the intrinsic properties of the qubit–coupler system. In this approach, the coupler is driven into an excited state, which induces a frequency shift in the qubit due to the Lamb effect. This shift can lead to imperfections in the qubit X gate, thereby altering the qubit state and hence providing valuable information about the coupler spectrum.[57] However, this method is constrained by the configuration of the qubit gate and does not support continuous-wave measurements, which limits the efficiency and applicability.

In this paper, we propose an efficient scheme for characterizing the coupler spectrum without the need for additional readout resonators. The main idea lies in inducing sideband transitions[58,59] by applying two non-resonant drives to the qubit and coupler, thereby facilitating two-photon interactions and enabling the response of the coupler spectrum. We experimentally demonstrate this approach on a quantum chip featuring qubits integrated with symmetric couplers, which are specifically designed to explore novel signatures[60] in quantum simulation.[61] Both continuous-wave and pulsed measurement protocols are implemented to characterize the target coupler, successfully retrieving the coupler spectrum. Furthermore, using the coupler spectrum obtained by this method, we calibrate the frequency dependence of the effective coupling strength between two qubits interconnected by the coupler.

2. Protocol

We investigate a superconducting quantum processor architecture, illustrated in Fig. 1(a), consisting of six grounded transmons $\{Q_j\}$[43] interconnected via a network of eight tunable couplers denoted $\{C_{12}, C_{23}, C_{15}, C_{24}, C_{35}, C_{26}, C_{45}, C_{56}\}$. Here, C_{ij} capacitively couples transmons Q_i and Q_j. More details about our experimental setup, including information about the wiring diagram, are available in our previous work.[62] These couplers, which are a type of floating transmon,[42] serve as symmetric-type coupling elements.[63] Specifically, the couplers, facilitating non-neighboring qubit interactions, are realized through the airbridge fabrication technique.[29] Both the qubits and couplers are flux-tunable, with each consisting of two identical Josephson junctions, which, in theory, exhibit a zero-frequency minimum. The detailed design parameters are summarized in Table 1. To experimentally demonstrate the protocol, we focus on the specific interaction between qubit Q_6 and its associated tunable coupler C_{26}. The Hamiltonian can be expressed as

$$H_{\rm tc} = \sum_{j\in\{\rm q,c\}} \left[\omega_j a_j^\dagger a_j + \frac{\eta_j}{2} a_j^\dagger a_j^\dagger a_j a_j\right] + g_{\rm qc}\left(a_{\rm c}^\dagger a_{\rm q} + a_{\rm c} a_{\rm q}^\dagger\right), \quad (1)$$

where $a_j^\dagger$ (a_j) denotes the bosonic creation (annihilation) operator, ω_j is the corresponding frequency under the two-level approximation, η_j represents the anharmonicity, and $g_{\rm qc}$ characterizes the capacitive coupling strength between the qubit q and the coupler c.

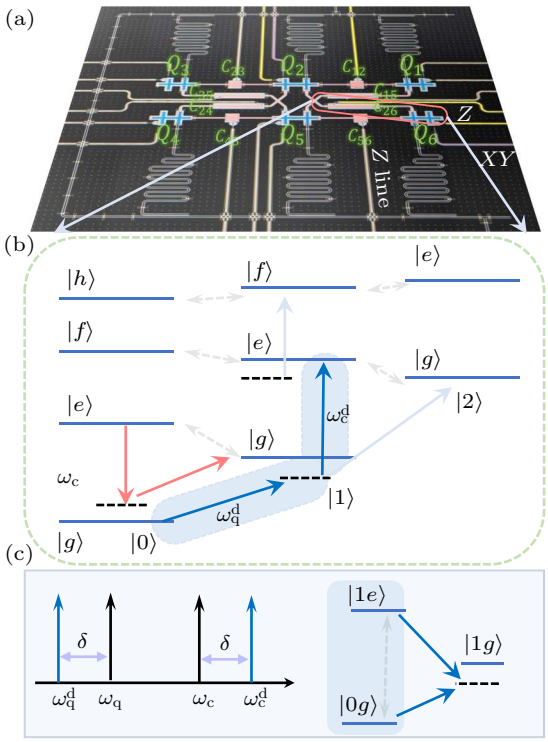


Fig. 1. (a) Enhanced connectivity of a 6-qubit (blue) superconducting quantum chip based on the transmon–coupler–transmon architecture. By flux-tuning the coupler (pink) frequency, high-contrast $XX+YY$ or ZZ interactions between qubits can be achieved. Each qubit has individual microwave lines (purple) for XY control, and the flux bias lines (yellow) for the coupler and qubit Z control. The coupler XY drive is mediated through the XY line of the coupled qubit. (b) Energy levels and schematic diagram for the example of Q_6 and C_{26}. By applying microwaves with a certain detuning frequency to both the qubit and coupler, the blue sideband driving is activated. (c) By applying detuned sideband frequencies $\omega_{\rm b}$ and $\omega_{\rm d}$ to the two lowest energy levels of the qubit, ω_{01}, and the coupler, ω_{ge}, the process is similar to the Ξ-system in coherent control. This enables effective coupling between the qubit and coupler, forming a subspace $\{|0g\rangle, |1e\rangle\}$, allowing the coupler state to be read out through the readout resonator.

In this scheme, the qubit is driven by an off-resonant ac-Stark tone via its individual microwave XY line at a fixed frequency $\omega_{\rm q}^{\rm d} = \omega_{\rm q} - \delta$, where δ denotes a small detuning from the qubit resonance. A second microwave tone is applied to the coupler near the frequency $\omega_{\rm c}^{\rm d} \simeq \omega_{\rm c} \pm \delta$, facilitating coherent two-photon transitions corresponding to either red or blue sidebands. As illustrated in Fig. 1(b), two-photon sideband transitions are generated by simultaneously driving the

qubit and coupler at $\omega_{\rm b} = \omega_{\rm c}^{\rm d} + \omega_{\rm q}^{\rm d}$ (known as the blue sideband) or $\omega_{\rm red} = \omega_{\rm c}^{\rm d} - \omega_{\rm q}^{\rm d}$ (referred to as the red sideband).

The effective Hamiltonians governing these interactions can be derived using perturbative methods,[64] yielding the following expressions for the red and blue sideband interactions:

$$H_{\rm 2R} \simeq \frac{g_{\rm qc}}{4}\frac{\Omega_{\rm c}}{\omega_{\rm c}-\omega_{\rm c}^{\rm d}}\frac{\Omega_{\rm q}}{\omega_{\rm c}-\omega_{\rm q}^{\rm d}}\left(a_{\rm c}^{\dagger}a_{\rm q}+a_{\rm c}a_{\rm q}^{\dagger}\right),$$
$$H_{\rm 2B} \simeq \frac{g_{\rm qc}}{4}\frac{\Omega_{\rm c}}{\omega_{\rm c}-\omega_{\rm c}^{\rm d}}\frac{\Omega_{\rm q}}{\omega_{\rm c}-\omega_{\rm q}^{\rm d}}\left(a_{\rm c}^{\dagger}a_{\rm q}^{\dagger}+a_{\rm c}a_{\rm q}\right), \qquad (2)$$

where the effective Rabi frequencies $\Omega_{\rm q}$ and $\Omega_{\rm c}$ are given by $\Omega_{\rm q,c} = 2g_{\rm qc}\varepsilon_{\rm q,c}/(\omega_{\rm q}-\omega_{\rm q,c}^{\rm d})$, with $\varepsilon_{\rm q,c}$ representing the drive amplitudes, which are small quantities during the spectral measurements. Thus, in our measurements, the coupler frequency affected by the drivings is neglected. By carefully tuning the qubit–coupler detuning and optimizing the relative amplitudes of the two driving tones, it is possible to achieve a high-contrast, strongly driven sideband transition, which is critical for precise characterization of the coupler.

Therefore, by applying two off-resonant microwave drives to the coupled qubit–coupler system, both red and blue sideband transitions can be coherently induced. The red sideband process corresponds to a transition from the state $|0e\rangle$ to $|1g\rangle$,[65] characterizing the coupler spectrum through the response of the qubit states. Here the first and second components in the state $|0e\rangle$ or $|1g\rangle$ represent the energy levels of the qubit and coupler, respectively (this notation is adopted throughout). Conversely, as shown in Fig. 1(c), the blue sideband transition selected in our experiment involves a transition from $|0g\rangle$ to $|1e\rangle$. The process is mediated via a virtual intermediate state and originates from drive-induced higher-order interactions, equivalent to the well-known coherent control applied in stimulated Raman passage.[66–68] As such, they effectively enlarge the accessible Hilbert space of the coupler. Specifically, the qubit–coupler subspace can be effectively redefined as $\{|0g\rangle, |1e\rangle\}$, where the states of the coupler ($|g\rangle$, $|e\rangle$) are conditionally mapped to the ground ($|0\rangle$) and excited ($|1\rangle$) states of the qubit, respectively. This conditional mapping enables the use of the qubit's readout resonator for dispersive measurement of the coupler state, providing a high-fidelity, indirect probing mechanism for characterizing the coupler dynamics within the extended Hilbert space.

Table 1. Designed parameters.

	Q_2	C_{26}	Q_6
Readout frequency, $\omega_{\rm r}/2\pi$ (GHz)	7.10	–	7.20
Sweet spot, $\omega^{\rm max}/2\pi$ (GHz)	4.0	4.5	4.0
Anharmonicity, $\eta/2\pi$ (MHz)	–235	–320	–272
Coupling strength*, $g_{\rm qc}/2\pi$ (MHz)	–66	–70	
Coupling strength*, $g_{26}/2\pi$ (MHz)	–2.76		
Coupling-off spot*, $\omega_{\rm c}/2\pi$ (GHz)	2.80		

*Calculated at the qubit frequency $\omega_0/2\pi = 3.825$ GHz.

3. Experimental results

First, all other qubits and couplers are flux-biased to the minimum of their respective spectral ranges in order to minimize their influence on the control and measurement of qubit Q_6 and coupler C_{26}. The resonance frequency of Q_6 and its readout contrast are characterized via its readout resonator. As depicted in Fig. 2(a), a carefully selected flux bias point is applied to coupler C_{26}, and two microwave drives are introduced according to the above protocol to facilitate the measurement of the coupler spectrum via sideband driving. Specifically, a detuning δ is introduced to the qubit drive frequency $\omega_{\rm q}^{\rm d}$, while a microwave tone at frequency $\omega_{\rm c}^{\rm d}$ is applied to the coupler.

We note that conventional couplers lack dedicated XY control and support only Z-driven operations. The coupler XY drive, with a small strength $\varepsilon_{\rm c}$, can be implemented either through the transmission line or via the qubit XY line. In our experiment, we implement direct XY driving for the coupler via the qubit XY line, facilitated by the strong qubit–coupler interaction. Notably, with careful circuit design, the coupler Z line can be repurposed for XY driving, thus obviating the need for additional components for sideband driving.

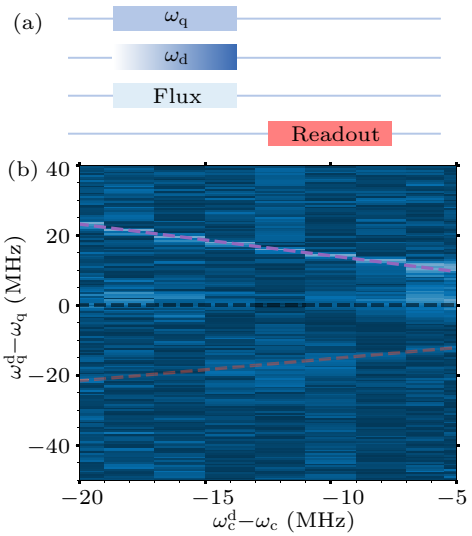


Fig. 2. (a) Coupler energy spectrum measurement based on sideband driving. A specific detuning δ is applied to the qubit drive frequency $\omega_{\rm q}$. Simultaneously, a microwave drive $\omega_{\rm c}$ is applied to the coupler for measurement purposes. This microwave drive can be realized either through a transmission line, the qubit XY line, or directly via the coupler flux line. The energy spectrum of the coupler is measured through the qubit readout resonator at a specific flux bias. (b) The corresponding coupler energy spectrum is measured for different detuning values δ of the drives. According to $\omega_{\rm q}^{\rm d} + \omega_{\rm c}^{\rm d} \simeq \omega_{\rm c} + \omega_{\rm q}$ for the blue sideband dirving, indicated by purple dashed line, the coupler spectrum is inferred from the response of the readout signal, which is a function of the detuning δ.

Accordingly, as shown in Fig. 2(b), the coupler spectrum is acquired as a function of the detuning parameter δ applied to $\omega_{\rm q}^{\rm d}$. The results, particularly the blue sideband transition indicated by the dashed purple line, exhibit a clear dependence on δ. From this response, the coupler drive frequency is inferred using the relation $\omega_{\rm c}^{\rm d} = \omega_{\rm c} + \delta$, thereby reconstructing

the coupler spectrum ω_c. Notably, residual excitations are observed in both the qubit and the coupler, which are most likely attributed to thermal population induced by the surrounding environment. This is evidenced by the appearance of red sideband transitions, shown as the red dashed line in Fig. 2(b), which are simultaneously present in the measurement.

To fully characterize the coupler spectrum under varying flux bias conditions, it is crucial to concurrently map the qubit spectrum as a function of the flux bias applied to the target coupler C_{26}. As illustrated in Fig. 3(a), the qubit spectrum shows a clear dependence on the flux bias of the coupler. The coupling strength between qubit Q_6 and coupler C_{26} is quantified as $|g_{6c}|/2\pi = 75$ MHz, with a resonant frequency of $\omega_0/2\pi = 3.825$ GHz. In the dispersive regime, where the coupling strength $g(\omega_c)$ is much smaller than the detuning between the qubit and coupler frequencies, i.e., $g(\omega_c) \ll |\omega_0 - \omega_c|$, and $g(\omega_c) = g_{6c}\sqrt{\omega_c/\omega_0}$, the predicted qubit spectrum is shown as dashed lines. This spectrum shift, induced by variations in the flux bias, also facilitates an approximate determination of the coupler spectrum by analyzing the readout resonator response.

Through sideband driving, as depicted in Fig. 3(b), the qubit drive frequency is fixed at $\omega_q^d/2\pi = 3.81$ GHz. A conventional pulse sequence in qubit spectroscopy measurements is employed. The resulting spectrum reveals a high-contrast spectral variation, indicating the coupler response to the applied drive. However, as highlighted in Fig. 3(a), the qubit spectrum experiences a shift, resulting in a change in the detuning δ of the sideband drive. This shift must be accounted for to accurately infer the true coupler spectrum. The corrected coupler spectrum, derived by considering this detuning, is illustrated by the pink dashed line.

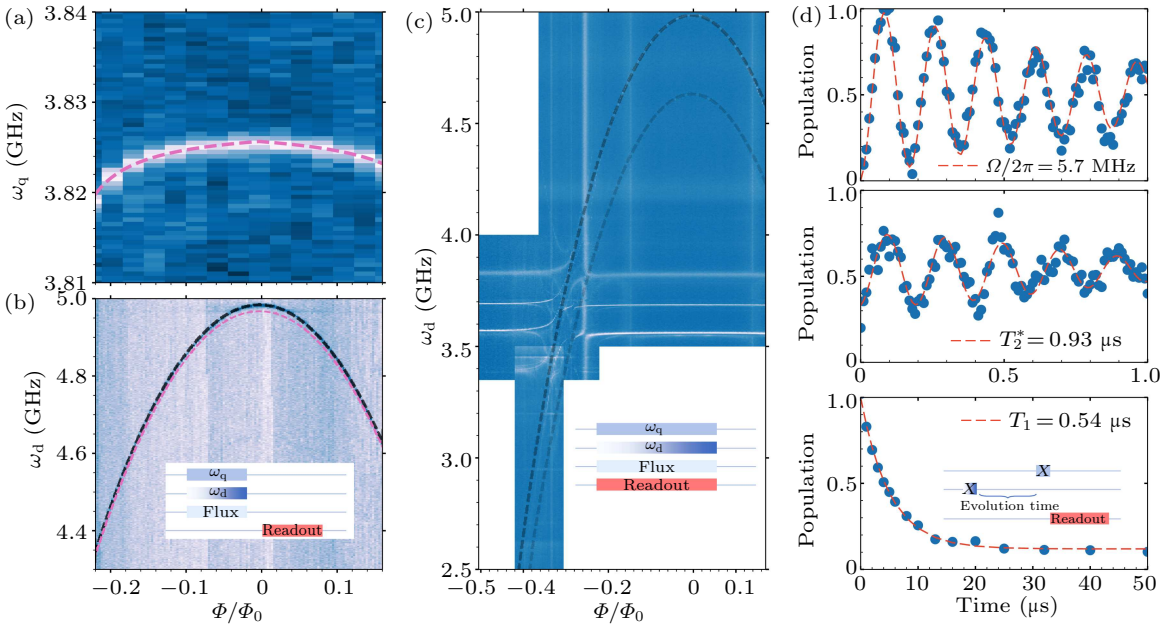


Fig. 3. (a) The energy spectrum of Q_6 varies as a function of the flux bias applied to the target coupler C_{26}. The coupling strength between the qubit and the coupler is $|g_{6c}|/2\pi = 75$ MHz at resonant frequency 3.825 GHz. According to Eq. (1), the theoretically predicted spectrum is shown as dashed lines. Conversely, this spectrum shift also allows for a rough estimation of the coupler spectrum. (b) Through sideband driving, the qubit drive frequency is fixed at $\omega_q^d/2\pi = 3.81$ GHz. A conventional qubit spectroscopy pulse sequence is applied with frequency sweeping. The resulting qubit response exhibits a high-contrast spectral variation. Taking the qubit freqcuency shift into account, the true energy spectrum of the coupler can be inferred and is illustrated by the pink dashed line. (c) Sideband driving is directly characterized using a VNA for continuous-wave spectroscopy. Three-tone continuous microwaves for readout resonator, qubit and coupler drivings are applied simultaneously. This setup enables direct measurement of the coupler spectrum across a wide modulation range, from 4.9 GHz down to 2.5 GHz. Due to the thermal occupation in the excited state, the f_{12} transition of the coupler is observable. The anharmonicity of the coupler is estimated to be $|\eta_c|/2\pi = 353$ MHz, which is consistent with the design. (d) Time-domain measurements are performed to calibrate the coherence properties of the coupler. From top to bottom, the panels show Rabi oscillations, a Ramsey interference experiment, and a T_1 relaxation measurement of the coupler. These results demonstrate that the coupler spectral and coherence properties can be characterized through the readout resonator of the coupled qubit.

Sideband driving can also be directly characterized using a vector network analyzer (VNA) in continuous-wave spectroscopy mode. In the experimental sequence, as illustrated in Fig. 3(c), three-tone continuous microwaves are applied simultaneously: one tone for the readout drive and two additional tones for the sideband drives associated with the qubit and the coupler. This configuration facilitates the direct measurement of the coupler spectrum over a broad modulation range, spanning from 4.9 GHz down to 2.5 GHz. Due to the finite thermal population in the coupler, the f_{12} transition of the coupler is also observable. From the data, we estimate the anharmonicity of the coupler to be $|\eta_c|/2\pi = 353$ MHz, which is in agreement with the design specifications that $|\eta_c|/2\pi = 320$ MHz.

However, to characterize the coherence properties of the

coupler via time-domain measurements, we have to employ calibrated pulse sequences; for instance, the T_1 measurement protocol is shown in the inset figure. In these sequences, a control pulse is first applied to the coupler, implementing the standard characterization routinely, and then another pulse is applied to the qubit followed by the readout. This approach ensures that the pulses are not applied simultaneously, avoiding the decaying process involving both qubit and coupler. As shown in Fig. 3(d), the panels, from top to bottom, present Rabi oscillations, a Ramsey interference experiment, and a T_1 relaxation measurement of the coupler. At the coupler's sweet spot, we obtain a T_1 value of 5.04 μs and a T_2^* value of 0.93 μs. These results provide a comprehensive characterization of both the spectral and coherence properties of the coupler, which can be directly assessed through the readout of the coupled qubit.

After characterizing the coupler spectrum, we proceed to quantify the effective inter-qubit coupling strength J. To this end, qubit Q_2 is capacitively coupled to the tunable coupler C_{26}, with a measured coupling strength of $|g_{2c}|/2\pi =$ 72.8 MHz at the resonance frequency ω_0. The system Hamiltonian can be expressed as

$$H_{\rm tct} = \sum_{j=2,6,c}\left[\omega_j a_j^\dagger a_j + \frac{\eta_j}{2}a_j^\dagger a_j^\dagger a_j a_j\right] + \sum_{j=2,6} g_{jc}(a_j^\dagger a_c + a_j a_c^\dagger) + g_{26}(a_6^\dagger a_2 + a_6 a_2^\dagger). \quad (3)$$

Under the dispersive regime, where $|\Delta_{jc}| \gg g_{jc}, g_{26}$, a Schrieffer–Wolff transformation yields the effective qubit–qubit coupling strength

$$J = \frac{g_{2c}g_{6c}}{2}\left(\frac{1}{\Delta_{2c}} + \frac{1}{\Delta_{6c}}\right) + g_{26}, \quad (4)$$

where $\Delta_{jc} \equiv \omega_j - \omega_c$. Circuit analysis indicates that $g_{26} < 0$ due to direct capacitive coupling between the qubits.[63] Consequently, the coupling cancellation occurs when the coupler frequency ω_c is biased below the qubit frequency. As shown in Fig. 4(a), biasing C_{26} to its minimum spot that is $\Phi/\Phi_0 = -0.5$, corresponding to $\omega_c/2\pi < 2.5$ GHz illustrated in Fig. 3(c), results in a vacuum Rabi pattern with a distinct tunable coupling signature.

The Rabi oscillations presented in Fig. 4(a) are fitted to extract the effective coupling strength as a function of the coupler frequency, previously characterized in Fig. 3(c). Utilizing the directly measured coupling strengths J and the coupler parameters at $\omega_q/2\pi = 3.825$ GHz, where $|g_{2c}|/2\pi = 72.8$ MHz and $|g_{6c}|/2\pi = 75.0$ MHz, and taking into account the symmetric coupling architecture between the qubits, the direct coupling strength between the two qubits is inferred to be $|g_{26}|/2\pi = 2.9$ MHz. This value is consistent with the theoretical prediction from Eq. (4), as illustrated in Fig. 4(b). The results confirm the successful implementation of a tunable coupling interface with a high on/off ratio.

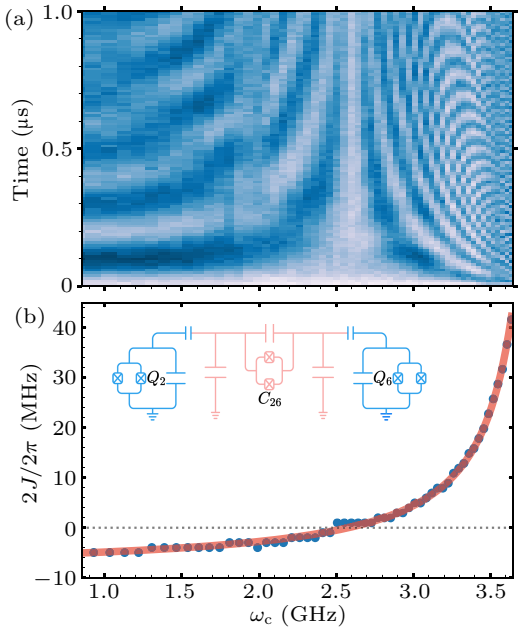


Fig. 4. (a) Both Q_2 and Q_6 are biased at a frequency of $\omega_q/2\pi =$ 3.825 GHz, while the coupler is initially positioned near its minimum, with a frequency inferred below 2.435 GHz at bias $\Phi/\Phi_0 = -0.5$. Q_6 is prepared in the excited state, and vacuum Rabi oscillations between the two qubits are measured. By controlling the flux bias of the coupler during the vacuum Rabi evolution, a Chevron pattern is obtained. (b) The Rabi oscillations are fitted to extract the effective coupling strength as a function of the coupler frequency. According to Eq. (4), considering that the two qubits are coupled through a symmetric coupling structure, the direct coupling strength between the two qubits is inferred to be $|g_{26}|/2\pi = 2.9$ MHz.

4. Conclusions

We have demonstrated a sideband transition technique that enables efficient characterization of the coupler spectrum within conventional transmon–coupler–transmon architectures. Experimental validation on a six-qubit device, employing both continuous-wave and pulsed measurement protocols, yielded the coupler spectrum. Meanwhile, we calibrate the frequency dependence of the effective coupling strength between two qubits, a key parameter for high-fidelity gates. This efficient characterization approach minimizes measurement overhead, facilitates rapid feedback for mitigating frequency crowding, and is immediately applicable across existing scalable quantum processor designs.

Acknowledgements

This work was partially supported by the Innovation Program for Quantum Science and Technology (Grant Nos. 2021ZD0301702 and 2024ZD0302000), the Natural Science Foundation of of Jiangsu Province (Grant No. BK20232002), the National Natural Science Foundation of China (Grant Nos. U21A20436 and 12074179), the Natural Science Foundation of Shandong Province (Grant No. ZR2023LZH002), and Nanjing University–China Mobile Communications Group Co., Ltd. Joint Institute.

References

[1] Yan F, Krantz P, Sung Y, Kjaergaard M, Campbell D L, Orlando T P, Gustavsson S and Oliver W D 2018 *Phys. Rev. Appl.* **10** 054062
[2] Mundada P, Zhang G, Hazard T and Houck A 2019 *Phys. Rev. Appl.* **12** 054023
[3] Li R, Kubo K, Ho Y, Yan Z, Nakamura Y and Goto H 2024 *Phys. Rev. X* **14** 041050
[4] Xu Y, Chu J, Yuan J, Qiu J, Zhou Y, Zhang L, Tan X, Yu Y, Liu S, Li J, *et al*. 2020 *Phys. Rev. Lett.* **125** 240503
[5] Sung Y, Ding L, Braumüller J, *et al*. 2021 *Phys. Rev. X* **11** 021058
[6] Stehlik J, Zajac D M, Underwood D L, Phung T, Blair J, Carnevale S, Klaus D, Keefe G A, Carniol A, Kumph M, Steffen M and Dial O E 2021 *Phys. Rev. Lett.* **127** 080505
[7] McKay D C, Filipp S, Mezzacapo A, Magesan E, Chow J M and Gambetta J M 2016 *Phys. Rev. Appl.* **6** 064007
[8] Foxen B, Neill C, Dunsworth A, *et al*. 2020 *Phys. Rev. Lett.* **125** 120504
[9] Chen Z, Liu W, Ma Y, Sun W, Wang R, Wang H, Xu H, Xue G, Yan H, Yang Z, Ding J, Gao Y, Li F, Zhang Y, Zhang Z, Jin Y, Yu H, Chen J and Yan F 2025 arXiv:2502.03612 [quant-ph]
[10] You J Q and Nori F 2011 *Nature* **474** 589
[11] Krantz P, Kjaergaard M, Yan F, Orlando T P, Gustavsson S and Oliver W D 2019 *Appl. Phys. Rev.* **6** 021318
[12] Blais A, Grimsmo A L, Girvin S M and Wallraff A 2021 *Rev. Mod. Phys.* **93** 025005
[13] Arute F, Arya K, Babbush R, Bacon D, Bardin J C, Barends R, Biswas R, Boixo S, Brandao F G, Buell D A, *et al*. 2019 *Nature* **574** 505
[14] Wu Y, Bao W S, Cao S, Chen F, Chen M C, Chen X, Chung T H, Deng H, Du Y, Fan D, *et al*. 2021 *Phys. Rev. Lett.* **127** 180501
[15] Gao D, Fan D, Zha C, *et al*. 2025 *Nature* **638** 920
[16] Ai G Q and Collaborators 2025 *Nature* **638** 920
[17] Shor P W 1997 arXiv:quant-ph/9605011
[18] Jiang L, Taylor J M, Sørensen A S and Lukin M D 2007 *Phys. Rev. A* **76** 062323
[19] Gambetta J M, Chow J M and Steffen M 2017 *npj Quantum Inf.* **3** 2
[20] Bravyi S, Dial O, Gambetta J M, Gil D and Nazario Z 2022 *J. Appl. Phys.* **132** 160902
[21] Ang J, Carini G, Chen Y, *et al*. 2022 (Preprint 2212.06167)
[22] Field M, Chen A Q, Scharmann B, Sete E A, Oruc F, Vu K, Kosenko V, Mutus J Y, Poletto S and Bestwick A 2024 *Phys. Rev. Appl.* **21** 54063
[23] Preskill J 2018 *Quantum* **2** 79
[24] Wang C, Li X, Xu H, Li Z, Wang J, Yang Z, Mi Z, Liang X, Su T, Yang C, Wang G, Wang W, Li Y, Chen M, Li C, Linghu K, Han J, Zhang Y, Feng Y, Song Y, Ma T, Zhang J, Wang R, Zhao P, Liu W, Xue G, Jin Y and Yu H 2022 *npj Quantum Inf.* **8** 3
[25] Tong H M, Lai Y S and Wong C 2013 *Advanced flip chip packaging* Vol. 142 (Springer)
[26] Kosen S, Li H X, Rommel M, *et al*. 2022 *Quantum Sci. Technol.* **7** 035018
[27] Koster N, Koblowski S, Bertenburg R, Heinen S and Wolff I 1989 Investigations on air bridges used for mmics in cpw technique *1989 19th European Microwave Conference* (IEEE) pp. 666–671
[28] Chen Z, Megrant A, Kelly J, Barends R, Bochmann J, Chen Y, Chiaro B, Dunsworth A, Jeffrey E, Mutus J, *et al*. 2014 *Appl. Phys. Lett.* **104** 052602
[29] Sun Y, Ding J, Xia X, Wang X, Xu J, Song S, Lan D, Zhao J and Yu Y 2022 *Appl. Phys. Lett.* **121** 074001
[30] Gambino J P, Adderly S A and Knickerbocker J U 2015 *Microelectron. Eng.* **135** 73
[31] Yost D R W, Schwartz M E, Mallek J, Rosenberg D, Stull C, Yoder J L, Calusine G, Cook M, Das R, Day A L, *et al*. 2020 *npj Quantum Inf.* **6** 59
[32] Gong M, Wang S, Zha C, Chen M C, Huang H L, Wu Y, Zhu Q, Zhao Y, Li S, Guo S, *et al*. 2021 *Science* **372** 948
[33] Chu J, He X, Zhou Y, Yuan J, Zhang L, Guo Q, Hai Y, Han Z, Hu C K, Huang W, *et al*. 2023 *Nat. Phys.* **19** 126
[34] Zhang X, Jiang W, Deng J, Wang K, Chen J, Zhang P, Ren W, Dong H, Xu S, Gao Y, Jin F, Zhu X, Guo Q, Li H, Song C, Gorshkov A V, Iadecola T, Liu F, Gong Z X, Wang Z, Deng D L and Wang H 2022 *Nature* **607** 468
[35] Xu S, Sun Z Z, Wang K, *et al*. 2023 *Chin. Phys. Lett.* **40** 060301
[36] Fowler A G, Mariantoni M, Martinis J M and Cleland A N 2012 *Phys. Rev. A* **86** 032324
[37] Cohen L Z, Kim I H, Bartlett S D and Brown B J 2022 *Sci. Adv.* **8** eabn1717
[38] Breuckmann N P and Eberhardt J N 2021 *PRX Quantum* **2** 040101
[39] Bravyi S, Cross A W, Gambetta J M, Maslov D, Rall P and Yoder T J 2024 *Nature* **627** 778
[40] Gidney C, Newman M, Brooks P and Jones C 2025 *Nat. Commun.* **16** 4498
[41] Wang K, Lu Z, Zhang C, *et al*. 2025 arXiv:2505.09684 [quant-ph]
[42] Koch J, Yu T M, Gambetta J, Houck A A, Schuster D I, Majer J, Blais A, Devoret M H, Girvin S M and Schoelkopf R J 2007 *Phys. Rev. A* **76** 042319
[43] Barends R, Kelly J, Megrant A, Sank D, Jeffrey E, Chen Y, Yin Y, Chiaro B, Mutus J, Neill C, O'Malley P, Roushan P, Wenner J, White T C, Cleland A N and Martinis J M 2013 *Phys. Rev. Lett.* **111** 080502
[44] Zhao P, Zhang Y, Xue G, Jin Y and Yu H 2022 *Appl. Phys. Lett.* **121** 32601
[45] Zhao C, He Y, Geng X, He K, Dai G, Liu J and Chen W 2023 *Chin. Phys. Lett.* **40** 010301
[46] Mollenhauer M, Irfan A, Cao X, Mandal S and Pfaff W 2024 (Preprint 2407.16743)
[47] Song J, Yang S, Liu P, Xue G M, Mi Z Y, Zhang W G, Yan F, Jin Y R and Yu H F 2024 (Preprint 2407.20338)
[48] Deng X, Zheng W, Liao X, Zhou H, Ge Y, Zhao J, Lan D, Tan X, Zhang Y, Li S and Yu Y 2025 *Phys. Rev. Lett.* **134** 020801
[49] Xiong H, Wang J, Song J, Yang J, Bao Z, Li Y, Mi Z Y, Zhang H, Yu H F, Song Y and Duan L 2025 (Preprint 2502.18902)
[50] Heya K, Phung T, Malekakhlagh M, Steiner R, Turchetti M, Shanks W, Mamin J, Lu W S, Kandel Y P, Sundaresan N and Orcutt J 2025 (Preprint 2502.15034)
[51] Xu J, Deng X, Zheng W, Yan W, Zhang T, Zhang Z, Huang W, Xia X, Liao X, Zhang Y, Zhao J, Li S, Tan X, Lan D and Yu Y 2025 arXiv:2506.14128 [quant-ph]
[52] Zhao P, Linghu K, Li Z, Xu P, Wang R, Xue G, Jin Y and Yu H 2022 *PRX Quantum* **3** 020301
[53] Zhang Y, Zhang Y, Li S, Zheng W and Yu Y 2024 *Chin. Phys. B* **33** 110306
[54] Wang R, Zhao P, Jin Y and Yu H 2022 *Appl. Phys. Lett.* **121** 152602
[55] Li T M, Zhang J C, Chen B J, Huang K, Liu H T, Xiao Y X, Deng C L, Liang G H, Chen C T, Liu Y, Li H, Bao Z T, Zhao K, Xu Y, Li L, He Y, Liu Z H, Yu Y H, Zhou S Y, Liu Y J, Song X, Zheng D, Xiang Z, Shi Y H, Xu K and Fan H 2025 *Phys. Rev. Appl.* **23** 024059
[56] Chu J and Yan F 2021 *Phys. Rev. Appl.* **16** 054020
[57] Xu H, Liu W, Li Z, Han J, Zhang J, Linghu K, Li Y, Chen M, Yang Z, Wang J, Ma T, Xue G, Jin Y and Yu H 2021 *Chin. Phys. B* **30** 044212
[58] Wallraff A, Schuster D I, Blais A, Gambetta J M, Schreier J, Frunzio L, Devoret M H, Girvin S M and Schoelkopf R J 2007 *Phys. Rev. Lett.* **99** 050501
[59] Chen Z, Wang Y, Li T, Tian L, Qiu Y, Inomata K, Yoshihara F, Han S, Nori F, Tsai J S and You J Q 2017 *Phys. Rev. A* **96** 012325
[60] Zhu Y Q, Zheng W, Zhu S L and Palumbo G 2021 *Phys. Rev. B* **104** 205103
[61] Georgescu I M, Ashhab S and Nori F 2014 *Rev. Mod. Phys.* **86** 153
[62] Zheng W, Xu J, Ma Z, Li Y, Dong Y, Zhang Y, Wang X, Sun G, Wu P, Zhao J, Li S, Lan D, Tan X and Yu Y 2022 *Chin. Phys. Lett.* **39** 100202
[63] Sete E A, Chen A Q, Manenti R, Kulshreshtha S and Poletto S 2021 *Phys. Rev. Appl.* **15** 064063
[64] Blais A, Gambetta J, Wallraff A, Schuster D I, Girvin S M, Devoret M H and Schoelkopf R J 2007 *Phys. Rev. A* **75** 032329
[65] It is note that this red sideband process, including two detuned XY drivings inducing a coherent interaction in redefined subaspace $\{|0e\rangle, |1g\rangle\}$, differs from the parametric modulation by using a low-frequency parametric drive on the Z control (flux bias) line to achieve an effective exchange interaction.[69]
[66] Li D, Zheng W, Chu J, Yang X, Song S, Han Z, Dong Y, Wang Z, Yu X, Lan D, Zhao J, Li S, Tan X and Yu Y 2021 *Appl. Phys. Lett.* **118** 104003
[67] Zheng W, Zhang Y, Dong Y, Xu J, Wang Z, Wang X, Li Y, Lan D, Zhao J, Li S, Tan X and Yu Y 2022 *npj Quantum Inf.* **8** 9
[68] Vitanov N V, Rangelov A A, Shore B W and Bergmann K 2017 *Rev. Mod. Phys.* **89** 015006
[69] Chu J, Li D, Yang X, Song S, Han Z, Yang Z, Dong Y, Zheng W, Wang Z, Yu X, Lan D, Tan X and Yu Y 2020 *Phys. Rev. Appl.* **13** 064012